PPPL-2264

I-24512

PPPL-2264

UC20-F

178
1/15/86

(2)

(24)

PPPL--2264

DE86 005037

SOME EFFECTS OF MHD ACTIVITY ON IMPURITY TRANSPORT IN THE PBX TOKAMAK

By

K. Ida, R.J. Fonck, R.A. Hulse, and B. LeBlanc

OCTOBER 1985

PLASMA PHYSICS LABORATORY

PRINCETON UNIVERSITY

PRINCETON, NEW JERSEY

PREPARED FOR THE U.S. DEPARTMENT OF ENERGY,
UNDER CONTRACT DE-AC02-76-CHO-3073.

SOME EFFECTS OF MHD ACTIVITY ON IMPURITY TRANSPORT IN THE PBX TOKAMAK

K. IDA*, R.J. FONCK, R.A. HULSE, and B. LEBLANC

Plasma Physics Laboratory

Princeton University

Princeton, New Jersey 08544

ABSTRACT

The effects of MHD activity on intrinsic impurity transport are studied in ohmic discharges of the Princeton Beta Experiment (PBX) by measuring of the Z_{eff} profile from visible bremsstrahlung radiation and the spectral line intensities from ultraviolet spectroscopy. A diffusive/convective transport model, including an internal disruption model, is used to simulate the data. The Z_{eff} profile with no MHD activity is fitted with a strong inward convection, characterized by a peaking parameter c_v ($= -a^2v/2rD$) = 11 (-3.5, +4.5). At the onset of MHD activity (a large m = 1 n = 1 oscillation followed by sawteeth), this strongly peaked profile is flattened and subsequently reaches a new quasi-equilibrium shape. This profile is characterized by reduced convection [c_v = 3.6 (-1.1, +1.6), D = 1.4 (-0.7, +5.6) $\times 10^4$ cm^2/s], in addition to the particle redistribution which accompanies the sawtooth internal disruptions.

*Permanent Address: Department of Physics, Faculty of Science, University of Tokyo, Bunkyo-ku, Tokyo 113, Japan

1. INTRODUCTION

The transport of impurities in tokamak plasmas is an important subject in nuclear fusion research. The effects of impurities on power balance, current density profile, and consequently, MHD activity have been emphasized. However, the relationship between MHD activity and impurity transport has not been studied in depth, in spite of its importance. Dynamic impurity behavior in so-called type-O and type-S discharges was observed in Doublet III,[1] where it was suggested that the impurity diffusion coefficient might be changed due to a large m=1, n=1 oscillation in the type-O discharges. Long impurity confinement times for Si were observed in an impurity injection experiment in ISX-B,[2,3] and these confinement times were significantly reduced by strong MHD activity. In the Poloidal Divertor Experiment (PDX) circular plasmas,[4] central titanium radiation (Ti XIX), during the steady-state portion of a discharge, was observed to be a factor 10-15 less in discharges with sawteeth than discharges without sawteeth. The effects of sawteeth on impurity transport have recently been the subject of comparison between sawtooth models and experimental observations. On Alcator-C,[5] a flat redistributed profile, which occurs after the internal disruption has been adopted to model soft X-ray measurements. In addition, the TFR group[6] has suggested that an outward convective velocity during the internal disruption phase itself could be used to simulate the linear increase of the Ni XXV line brightness during the recovery phase of the sawtooth oscillation.

In general, a detailed analysis of impurity transport effects with MHD activity has been hindered by the lack of sufficiently complete information on the spatial distribution of the total impurity density. The few measurements which do exist show a variety of impurity behavior in various experiments for ohmically heated plasmas. Using visible bremsstrahlung measurements,[7] a peaked Z_{eff} profile in the high density regime was observed in JIPPT-II, while flat Z_{eff} profiles were observed in Alcator-C and PDX. Fully ionized low-Z impurity profiles were measured by charge-exchange recombination spectroscopy[8] in PDX.[9] While the profiles of $n_{O^{8+}}$ and $n_{C^{6+}}$ were slightly more peaked than $n_e(r)$, these results were consistent with no significant peaking of Z_{eff} on axis. A He^{++} transport study[10] derived a diffusion coefficient in the range of 1.2×10^4 to 3.0×10^4 cm^2/s for ohmically heated PDX discharges and indicated that, roughly, $n_{He^{++}} \propto n_e$. These PDX results were obtained for plasmas with no discernable MHD activity.

In this paper, we discuss observations of the effects of the onset of sawtooth oscillations on gross impurity transport in the PBX tokamak. In the course of this effort, we discuss the determination of intrinsic impurity transport coefficients using a model including internal disruptions and a simple diffusive/convective flux model. In general, a sudden flattening of the Z_{eff} profile is observed at the onset of a large m=1, n=1 oscillation and its subsequent disruptions. This flattening is referred to as the "impurity crash" in this paper. The measured Z_{eff} profile is fitted using a peaking parameter c_v, which reflects the ratio of convective to diffusive transport terms, before and after the impurity "crash." After accounting for the direct mixing effects of the sawtooth, a significant difference of this peaking parameter is observed with and without MHD activity, indicating a change in the radial transport itself. Space- and time-resolved studies of impurities

using visible bremsstrahlung spectroscopy, coupled with plasma profiles obtained via Thomson scattering, allow the measurement of the radial profile of the total impurity density via the effective ion charge Z_{eff} without the large uncertainties in atomic processes which are common in conventional spectroscopic observations.

The steady-state Z_{eff} profile provides a unique ratio of convection to diffusion in transport equilibrium with no sawteeth, assuming all the dominant impurities experience the same transport. However, the Z_{eff} profile is not a unique function of this ratio with sawteeth present, but becomes a function of both the peaking parameter c_v and the diffusion coefficient D, given a fixed sawtooth period and mixing radius. The Z_{eff} profile thus provides a relationship between c_v and D inside the mixing radius. In addition, the decay time of Ni XVII and Ni XVIII line radiation during the "crash" provides another constraint on the allowed values of c_v and D in the content of the flux model. These simultaneous constraints on the relative values of the diffusive and convective terms provide, within large experimental uncertainties, absolute values of these transport terms for the time after the crash.

2. EXPERIMENTAL APPARATUS AND TECHNIQUE

The Princeton Beta Experiment (PBX) is a large tokamak (R = 1.45 m, a = 0.35 m, B_t = 1.4 T) in which the effects of a kidney-bean-shaped configuration are studied in high beta discharges.[11] Plasma indentation on the inboard side is produced by a "pusher" coil which is located on the midplane inside wall. The coil is protected from plasma and neutral beam impact by carbon graphite armor which covers ~30% of the coil surface. The plasma is limited by a

separatrix or by carbon limiters which are located at four different toroidal locations. Three sets of 2.5-cm thick Ni-coated aluminum plates are located near the bean lobes to stabilize gross MHD motion. For this study, ohmic discharges with $\bar{n}_e \approx 2.7 \times 10^{13}$ cm^{-3}, $I_p = 290$ kA, $q(a) = 7.7$, and $a = 35$ cm were produced with H^+ as the working gas. The plasma is initiated with a circular cross section, then translated to a smaller major radius to form the bean-shaped configuration shown in Fig. 1. Midplane observations with the SPRED multichannel vacuum ultraviolet (VUV) spectrometer[12,13] indicate that the dominant light impurities are carbon (from the limiters and armor) and oxygen, and that the dominant heavy impurity is nickel.

A visible bremsstrahlung detector array system (Fig. 1) was installed on PBX to provide a 15-channel midplane tangential view of the plasma in order to take advantage of the circular (i.e., toroidal) plasma symmetry in that field of view and to avoid regions of local recycling near the separatrix and inner armor. A standard 50-mm f/2 camera lens images the plasma onto the 15 optical fibers quartz (600 μm core diameter) that are arranged in a one-dimensional array on the focal plane. From there the optical train is identical to that used on the PDX device.[14] The collimated light is sent to a remote photomultiplier through two interference filters that are tilted with respect to one another to avoid undesirable cavity modes. One filter has a wide (40 Å) passband width while the other has a narrow (6 Å) width, and both are tuned to 5235 Å where an optical multichannel analyzer spectrum showed a spectral region free of discrete spectral lines. There is no viewing dump in this tangential view system, and the outermost channel views the wall outside the outer limiter flux surface. An extra channel with a viewing dump on a midplane radial view is used to cross-check for wall reflections and to monitor window transmittance. Since the tangentially viewing system has a

longer line of sight through the plasma than the previously used radial view, the ratio of diffuse wall-reflected light to the signal is reduced to less than 5%. This relatively uniform background signal is subtracted from all channels before the Abel inversion.

A multichannel (48-point) Thomson scattering system (TVTS) measures the radial electron temperature and density profiles in the same midplane as the tangentially viewing visible bremsstrahlung array. This avoids uncertainties due to the plasma cross-sectional shape and any asymmetric density or temperature profiles. Line-integrated signals from a tangential view allow simple Abel inversion techniques to be employed, regardless of plasma shape in the poloidal cross section. The Z_{eff} profile is calculated from the inverted emission profiles using the measured electron density and temperature profiles. Central carbon and oxygen concentrations are calculated using the ratio of carbon to oxygen, derived from plasma edge spectroscopic measurements, together with the total carbon and oxygen contribution to $Z_{eff}(0)$, derived by subtracting the directly measured contributions of nickel from the measured $Z_{eff}(0)$. A 28-channel soft X-ray diode array views the plasma vertically on a poloidal cross section to provide a monitor of MHD activity.

3. EXPERIMENTAL OBSERVATIONS

The time evolution of various signals relevant to the present experiment are shown in Fig. 2 for an ohmic discharge. The indentation field current I_{IF} is delayed by ~100 ms from the evolution of the plasma current I_p, and by ~180 ms a relatively steady-state bean-shaped plasma is achieved with an

indentation of i = 0.12. At some time well into the current flattop, rapid decreases in the central soft X-ray signal, central visible bremsstrahlung channel, and the Ni XVII and Ni XVIII emissions are observed. They coincide with the onset of a large oscillation observed with the soft X ray. The onset of this rapid decrease in central impurity levels and subsequent sawtooth oscillations in the plasma core, which we refer to here as the impurity "crash," occurs earlier in the discharge as the gas puffing level is increased. While additional gas puffing is expected to reduce impurity influx, it also helps increase current penetration[15,16] by reducing the temperature and conductivity in the plasma edge region, therefore, allowing $q(0) < 1$ to be attained earlier in the discharge. The penetration time of the poloidal magnetic field is estimated to be ~400 ms for PBX ohmic discharges.[15]

During the "crash," the chordally integrated soft X-ray emission profile shows internal disruptions, with an increasing inversion radius during the first three disruptions [Fig. 3(a)]. After the "crash" period, the soft X-ray emissions show regular sawtooth oscillations with a period of ~10 ms. A large m/n = 1/1 oscillation (f = 1.8 kHz) is observed between internal disruptions only in the "crash" phase, and this MHD activity differs from the normal precursor to internal disruptions in the following way: While the oscillation is localized within the inversion radius as shown in Fig. 3(b), its amplitude is more or less constant between internal disruptions until it is quickly stabilized before the next internal disruption. While the detailed mechanism for this activity is not yet understood, it is clear that it is observed only in this phase of the discharge.

The electron temperature profile is flat or slightly hollow in the center before and after the "crash" while the density profile is peaked in the plasma center before and flat afterwards, as seen in the Thomson scattering profiles

of Fig. 4. The peaked density profile experiences flattening at the same time as the soft X-ray profile and the visible bremsstrahlung profiles, which are shown in Fig. 5. Since the visible bremsstrahlung emissivity, which is proportional to $Z_{eff}n_e^2T_e^{-1/2}$, shows a flattening similar to that of the soft X-rays and the electron temperature profiles do not drastically change while the central electron density drops by ~ 25%, it appears that the drop in the X-ray intensity is due more to a decrease in the central impurity content than to the drop in electron temperature.

The Abel-inverted visible bremsstrahlung emissivity profiles are very peaked before the "crash" (which is obvious even in the chordal data) and relatively rounded after the "crash," in the normal sawtooth phase of the discharge. The measured Z_{eff} profiles are shown in Fig. 6 for the times before and after the crash. The Z_{eff} profile is found to be very peaked before the crash, Fig. 6(a), even after taking the peaked n_e profile into account. After the "crash," the Z_{eff} profile, averaged over a sawtooth period, was still slightly peaked on axis, but less so than before the "crash." The error bars on the data in Fig. 6 reflect only the uncertainties in the Abel-inverted emissivity profiles, due to a 5% relative calibration uncertainty in the visible bremsstrahlung detector array. The solid and dashed lines in Fig. 6 are results from the transport calculations described in the next section.

Due to low signal levels, the visible bremsstrahlung was averaged over a 10 ms period, precluding an observation of discrete sawtooth oscillations in the continuum radiation in these discharges. In later experiments with neutral beam injection at higher plasma densities, longer sawtooth periods, and often higher impurity levels, the signal-to-noise levels allowed observations of sawteeth directly in the bremsstrahlung emissivity profiles.

These profiles are almost flat after an internal disruption inside the inversion radius (as is the electron density) and become more peaked before the next sawtooth. These results will be discussed in detail in a later report.

4. TRANSPORT MODELING AND ANALYSIS

The one-dimensional radial impurity transport code MIST[17] has been used to analyze the time evolution of the impurity radiation and the Z_{eff} profiles discussed in the previous section. For simplicity, toroidal and poloidal symmetry are assumed in this code, and the governing equation for the radial distribution of a given charge state +q in space and time has the form:

$$\frac{\partial n_q}{\partial t} = -\frac{1}{r}\frac{\partial}{\partial r}(r\Gamma_q) + I_{q-1}\,n_{q-1} - (I_q + R_q)\,n_q \qquad (1)$$

$$+ R_{q+1}\,n_{q+1} - \frac{n_q}{\tau_\parallel} + S_q \,.$$

Here I_q and R_q are the total ionization and recombination rates for charge state q, respectively. $\tau_\parallel$ is a parallel loss time in the plasma scrape-off region, and S_q is a volume source term of recycled or injected impurity neutrals from the plasma edge region. The particle flux for charge state q is given by the general form

$$\Gamma_q = -D_q(r)\,\frac{\partial n_q}{\partial r} + v_q(r)\,n_q \,, \qquad (2)$$

where $D_q(r)$ is the radial diffusion coefficient and v_q is a convective velocity. Since in this experiment the character of the data precludes a detailed transport analysis and since we are most concerned with the peaking of the Z_{eff} profile, we simplify the transport model and define a peaking parameter c_v via the following expressions:

$$D_q(r) = D(r) = D \quad , \tag{3}$$

$$v_q(r) = v(r) = -c_v \frac{2Dr}{a^2} \quad , \tag{4}$$

where a is the plasma minor radius. In a steady-state plasma, the above definitions give a Gaussian equilibrium radial profile for the total impurity density in the source/sink-free core plasma region:

$$\Sigma\, n_q(r) \propto \exp\left(-c_v\, r^2/a^2\right) \quad . \tag{5}$$

The value of c_v, as defined above, thus indicates the power to which a Gaussian profile is raised to model the total impurity profile.

A time-dependent sawtooth model similar to that described by Seguin, Petrasso, and Marmar[5] has been incorporated into the MIST code to simulate impurity transport in the presence of internal disruptions. At the time of the internal disruption, the density profile for each charge state is redistributed inside a mixing radius r_{mix} while conserving the total number of

particles for each charge state, as illustrated in Fig. 7. The post-disruption total impurity density profile is adjustable, but chosen to be flat for our initial discussions (as indicated in Fig. 7). Assuming a nearly parabolic current density profile, r_{mix} is taken to be 1.4 times the sawtooth inversion radius r_{inv}.[18] After the redistribution, the charge states evolve according to Eqs. (1)-(4) until the next internal disruption. The assumption of a flat redistributed profile for each state may not be correct, but it is a reasonable first estimate. The sensitivity of the present analysis to the shape of the redistributed profile in this sawtooth model is discussed later.

In PBX ohmic discharges, Ni XVII (wavelength = 249.2 Å, ionizaton potential = 570 eV) and Ni XVIII (292.0 Å, 607 eV) radiate from the central half of the plasma minor radius, allowing near-central nickel concentrations to be measured directly. On the other hand, central oxygen and carbon concentrations could not be measured due to a lack of a diagnostic neutral beam for charge-exchange recombination spectroscopy measurements, and the highest spectrally accessible states were the lithiumlike ions CIV (312.4 Å, 65 eV) and O VI (150.1 Å, 138 eV), which radiate from the plasma edge region. While central impurity concentrations derived from edge radiation have large uncertainties due to transport and atomic physics uncertainties, it is reasonable for the present purposes to use these observed line intensities to estimate, via the transport code, the ratio of the edge influx of carbon to that of oxygen. Since previous measurements in PDX suggested similar transport for carbon and oxygen,[8] this modeling can be used to estimate the central carbon-to-oxygen ratio. Sensitivity studies using relatively wide variations in the diffusion coefficent D (from 0.5×10^4 to 2.0×10^4 cm^2/s), peaking parameter c_v (from 0.0 to 3.0), scrape-off parallel loss time $\tau_{\parallel}$ (from 0.4 to 10 ms), neutral particle energy E_n (from 0.1 to 10 eV), and impurity

source location r_s (from 0 to 10 cm from the plasma surface) indicate that the central carbon-oxygen ratio derived from these edge C IV, O VI line ratios have at most a 25% uncertainty due to transport assumptions.

In order to determine the value of the peaking factor c_v from the measured Z_{eff} profile, we assume that the three dominant impurity species (carbon, oxygen, and nickel) have the same transport coefficients and derive the relative contributions to $Z_{eff}(0)$ from estimates of the central impurity density ratios. The resultant central nickel concentration, as measured by Ni XVII and XVIII emissions, is 0.1% before and 0.01% after the "crash." Using the above-mentioned influx ratio to derive the central oxygen-to-carbon ratio and the value of $Z_{eff}(0)$ minus the nickel contribution gives 1.5% and 3.2% before and 0.6% and 2.1% after the crash for oxygen and carbon concentrations, respectively. The profiles of $Z_{eff}(r)$ are fitted by the results of the transport calculations, and using a least squares fitting of the data to the calculated profile which is normalized to the measured $Z_{eff}(0)$, the best fit to the profile before the "crash" gives $c_v = 11.0$. The resultant chi-squared per degree of freedom χ^2_ν is 0.39. We estimate the uncertainty in c_v by varying its value until χ^2_ν increases by one, which gives $c_v \approx 11.0$ (+4.5, -3.5) for the "before crash" case. The calculated profiles for the best fit case and the two extremes are shown in Fig. 6(a). We note that the "before crash" calculations are essentially steady-state profiles, although the rising visible continuum and soft X-ray signals would indicate that a quasi-steady-state condition has not necessarily been achieved before the onset of the "crash." However, this analysis is sufficient to demonstrate the need for a strong inward convective velocity to describe the peaked $Z_{eff}(r)$ profile.

Unlike the earlier studies in PDX with no sawteeth,[8,10] the quasi-steady-state impurity profile measurements in the sawtooth phase do not provide a

unique value of the peaking parameter c_v because the sawtooth redistribution effectively keeps the profiles out of transport equilibrium. On the average, the profile is determined by how fast the impurity distributions recover towards the transport equilibrium limit before the next internal disruption, which clearly depends on the diffusive and convective transport in the central discharge region. While the sensitivity of the derived value of c_v on the assumed D is discussed in detail below, it is clear that, in contrast to the above case, the Z_{eff} profile after the "crash" is considerably less peaked and lower in magnitude altogether. Averaging both the measurments and the modeling calculations over a sawtooth period (≈10 ms) gives c_v = 4.0 (+2.5, -1.5) as the best estimate of the peaking factor for D = 10^4 cm^2/s. Ignoring sawtooth effects altogether in the modeling gives c_v = 3.0. The calculated Z_{eff} profiles are shown in Fig. 6(b).

Figure 8 shows the effects of three different redistributed impurity profile assumptions on the sawtooth-modified Z_{eff} profile. Case I is the flat profile used in most of this analysis, while cases II and III represent more hollow redistributed impurity density profiles. These hollow profiles are qualitatively similar to those produced by a strong outward convection during the internal disruption, as discussed by the TFR group in their sawtooth modeling effort.[6] As Fig. 8 shows, Cases I or II are reasonably indistinguishable when analyzing the sawtooth-averaged Z_{eff} profile, and the resulting uncertainty in the adopted peaking parameter is relatively small compared with the uncertainty of the Z_{eff} profile measurements itself.

The measured time evolution of the Ni XVII 249.2 Å and Ni XVIII 292.0 Å line intensities show reasonable agreement with the code calculations within the estimated uncertainties of the c_v parameter during the sawtooth phase of the discharge, as shown in Fig. 9. Here, the measurements of the UV lines are

made with the multichannel SPRED spectrometer, which has a 20 ms integration time. The absolute intensity calibration was achieved with a branching ratio calibration,[19] and the uncertainty in the ratio of the Ni XVII and XVIII line intensities is ~10% from the spectrometer calibration.

To model the change in impurity distributions across the time of the "crash," we take the equilibrium impurity distributions for c_v = 11.0 and normalize them to the measured intensities at t = 450 ms. These resulting Ni ion distributions are used for the initial conditions of the time-dependent sequence, which starts at the onset of the internal disruptions at t = 490 ms, with a period of 10 ms. The calculated time evolutions of the Ni lines are shown in Fig. 9 for the estimated range of c_v during the sawtooth phase. The error bar on the calculated curves indicates uncertainties obtained using Thomson scattering profiles measured at t = 500, 520, 540, and 560 ms. The Ni influx rate after the "crash" is taken to be the same as that before the "crash." Since high c_v = 11 implies a long central confinement time for these ions, this influx rate is quite low (~2 × 10^{15} atoms/s for D = 10^4 cm^2/s). Increasing the influx rate after the "crash" by two orders of magnitude does not change the fitted transport coefficients, and the Ni XVII and XVIII calculated intensities rise by only 10% and saturate in time more quickly than observed. In general, the Ni emission lines are well described by the model, with parameters derived from the Z_{eff} profiles within the uncertainties of the c_v value and the line intensity calculations. Given the uncertainties in ionization and recombination rates, the simplicity of the diffusive/convective flux model, and the assumption that c_v is not a function of q, the agreement between the measured Ni XVII and XVIII intensities and the calculated values is quite reasonable.

Since fixed values of c_v and D produce a unique Z_{eff} profile and unique decay times of the Ni XVII and XVIII emissions during the "crash" phase, these measurements can be combined to estimate the range of c_v values allowed by the data during the "crash" and sawtoothing phase. A summary of how our relatively crude data constrains D and c_v is shown in Fig. 10, which also shows the range of c_v and D values allowed by our observations of the "crash" phase. The range of c_v and D pairs allowed by the Z_{eff} profile measurements is noted by the closed squares and solid and dashed lines in the figure [e.g., at D = 10^4 cm^2/s, c_v = 4.0 (+2.0, -1.5)]. To match a given Z_{eff} profile, an increased peaking factor is needed as D reduces to retain the same inward convection speed with reduced diffusive transport during a sawtooth period. Since an increased inward convection tends to decrease the decay of the Ni line emissions, D must be increased as c_v increases to model consistently the Ni line emissions. The constrained pairs of c_v, D allowed by the Ni XVII and XVIII emissions are noted by the open and closed circles, respectively. Likewise, the ratio of Ni XVII to XVIII intensities, which more or less describe a local slope of nickel impurities, constrain the values of c_v, D to a region similar to that given by the Z_{eff} profile.

The shaded intersection area indicates the allowed range of c_v, D consistent with both types of measurements in the sawtoothing plasma. While this crossed area gives a large range for D = 1.4 (-0.7, +5.6) × 10^4 cm^2/s and c_v = 3.6 (-1.1, +1.6), it is sufficiently constrained to exclude overlap with the c_v values required to describe the no MHD case. In addition, our uncertainty estimates on c_v from the fit to the Z_{eff} profile may be overly generous. Nonetheless, the range of the diffusion coefficient is consistent with the values obtained from earlier experiments on He^{++}, C^{6+}, O^{8+}, and Sc transport in PDX.[8,10,20] Taking D = 10^4 cm^2/s, the inward convective speed is

$v \approx 2.8 \times 10^3$ (r/a) cm/s, which is faster than the values of $v \approx 6.8 \times 10^2$ (r/a) cm/s (nickel), 2.5×10^2 (r/a) cm/s (oxygen) and 1.8×10^2 (r/a) cm/s (carbon) given by neoclassical theory in the Pfirsch-Schlüter regime assuming Gaussian T_i and n_i profiles.[21]

5. DISCUSSION

The most immediate conclusion to be drawn from the above observations is the obvious one: MHD behavior, in particular sawtooth oscillations, cannot be ignored when studying impurity transport in tokamak discharges. Indeed, even after subtracting out the sawtooth flattening effect, there appears to be a significant difference in impurity transport between a plasma with no MHD activity, such as before the "crash," and a discharge with MHD activity (both sawteeth and m/n = 1/1 oscillations). In the context of our simple transport model, the peaking parameter c_v with no MHD activity is large (≈11) while it is considerably smaller (≈3.6 for $D = 1.4 \times 10^4$ cm^2/s) in a sawtoothing discharge. While such a relation between impurity behavior and MHD activity has been discussed in other studies (e.g., Ref. 1, 5, and 6), the analysis of relatively global quantities such as the Z_{eff} profile allows a more quantitative evaluation of this phenomenon than hitherto shown in previous reports.

Finally, we note that the peaked Z_{eff} profiles in PBX, even in the presence of sawteeth, contrasts with the relatively flat Z_{eff} profiles seen in ohmic PDX and Alcator-C[22] discharges. Although impurity accumulation has been inferred from line intensity ratios in ISX-B,[2] the present data set explicitly shows a peaked impurity profile. The most curious difference lies between

these results on PBX and the flat Z_{eff} profiles and flat impurity concentration measurements[8,10] in the predecessor PDX device. Perhaps a relevant difference in operation between the two configurations is the biasing condition of the limiting surfaces. Unlike PBX, wherein all limiting surfaces are grounded, the carbon rail limiter and divertor neutralizer plates on PDX were floated above ground by 10 to 50 Ω, with the result that the plasma edge had a positive potential[23] with respect to the vessel wall. As shown in the Microtor device,[24] relatively small changes in the edge potential can cause drastic changes in impurity and particle confinement behavior. Indeed, very preliminary observations in PBX with a limiter grounded through 1 or 10 Ω indicate the impurity accumulation may be more severe for the 1 Ω case. Detailed tests of the limiter conditions on impurity confinement in PBX are planned for the near future and will be reported later.

Thus, while other effects such as edge conditions, rotation effects, background plasma species, etc. must all be taken into account in a complete treatment of impurity behavior, the present results serve to emphasize the very strong role of MHD activity, in particular sawtooth oscillations, in modifying both the distribution of impurity particles and, apparently, the transport processes themselves in the plasma core.

ACKNOWLEDGMENTS

The authors wish to thank M. Okabayashi, K. Bol, and the PBX team for their support during this work. Useful conversations with G. Jahns, R. Groebner, and M. Shimada are gratefully acknowledged. K. Itami provided the data from the soft X-ray wave detector. The authors thank B. Saoutic for a preliminary copy of the TFR sawtooth modeling results.

This work was supported by the U.S. Department of Energy, Contract No. DE-AC02-76-CHO-3073.

REFERENCES

1. G.L. Jahns, S. Ejima, R.J. Groebner, N.H. Brooks, et al., Nucl. Fusion 22 (1982) 1049.

2. K.H. Burrell, S.K. Wong, C.H. Muller, III, M.P. Hacker, H.E. Ketterer, R.C. Isler, E.A. Lazarus, Nucl. Fusion 21 (1981) 1009.

3. R.C. Isler, L.E. Murray, E.C. Crume, C.E. Bush, et al., Nucl. Fusion 23 (1983) 1017.

4. D. Meade et al., in Plasma Physics and Controlled Nuclear Fusion Research (Proc. 8th Int. Conf., Brussels, 1980) Vol. I, IAEA, Vienna (1981) 665.

5. F.H. Seguin, R. Petrasso, E.S. Marmar, Phys. Rev. Lett. 51 (1983) 455.

6. TFR Group, Association Euratom-CEA Sur La Fusion Report, EUR-CEA-FC-1255 (1985) 16 pp.

7. K. Kadota, M. Otsuka, J. Fujita, Nucl. Fusion 20 (1980) 209.

8. R.J. Fonck, M. Finkenthal, R.J. Goldston, D.L. Herndon, R.A. Hulse, R. Kaita, D.D. Meyerhofer, Phys. Rev. Lett. 49 (1982) 737.

9. R.J. Fonck, D.S. Darrow, K.P. Jaehnig, Phys. Rev. A 29 (1984) 3288.

10. R.J. Fonck and R.A. Hulse, Phys. Rev. Lett. 52 (1984) 530.

11. M. Okabayashi et al., in Plasma Physics and Controlled Nuclear Fusion Research 1984 (Proc. 10th Int. Conf., London, 1984) Vol. 1. IAEA, Vienna (1985) 229.

12. R.J. Fonck, A.T. Ramsey, R.V. Yelle, Appl. Opt. 21 (1982) 2115.

13. R.J. Fonck, in Multichannel Image Detectors, edited by Yair Talmi (American Chemical Society, Washington, D.C., 1983), Vol. 2, 277.

14. A.T. Ramsey, R.J. Fonck, R.W. Reeves, P.R. Thomas, Bull. Am. Phys. Soc 27 (1982) 823.

15. K. Toi, S. Itoh, K. Kadota, K. Kawahata, N. Noda, K. Sakurai, K. Sato, S. Tanahashi, S. Yasue, Nucl. Fusion 19 (1979) 1643.

16. R.D. Stambaugh, F.P. Blau, S. Ejima, G.L. Jahns, J.L. Luxom, M. Shimada, T.S. Taylor, R.E. Waltz, Nucl. Fusion 22 (1982) 395.

17. R.A. Hulse, Nuclear Technol./Fusion 3 (1983) 259.

18. B.B. Kadomtsev, Sov. J. Plasma Phys. 5 (1975) 389.

19. Equi e TFR, Nucl. Fusion 15 (1975) 1053.

20. R. Hulse, K. Brau, J. Cecchi, S. Cohen, M. Finkenthal, R.J. Fonck, D. Manos, S. Suckewer, Bull. Am. Phys. Soc. 26 (1981) 864.

21. P.H. Rutherford, Phys. Fluids 17 (1974) 1782.

22. M.E. Foord, E.S. Marmar, J.L. Terry, Rev. Sci. Instrum. 53 (1982) 1407.

23. R. Budny and D. Manos, J. Nucl. Mater. 121 (1984) 41.

24. L. Oren, L. Keller, F. Schwirzke, S. Talmadge, R.J. Taylor, J. Nucl. Mater. 111 & 112 (1982) 34.

FIGURE CAPTIONS

Fig. 1. Schematic diagram of the tangentially viewing visible bremsstrahlung spectroscopy array on PBX along with the toroidal location at the soft X-ray (SXR), Thomson scattering (TVTS), and VUV spectrometer (SPRED) diagnostics. The remote detector assembly, denoted by PMT, includes both the spectral filters and photomultiplier detectors. The inset shows a cross-sectional flux contour of a bean-shaped plasma limited on the inner graphite limiter.

Fig. 2. Time evolution of the plasma and indentation currents (I_p, I_{IP}), line integrated soft X-ray emission(SXR), visible bremsstrahlung, continuum (VC) and UV emissions. The sudden decrease ("crash") of impurity levels occurs at t = 485 ms.

Fig. 3. (a) Internal disruptions and (b) n=1 m=1 large oscillations observed by the soft X-ray line-integrated emission profile. An internal disruption occurs at t = 490 msec, followed by a large amplitude n=1 m=1 oscillation (f = 1.8 kHz) which stabilize at t = 515 msec.

Fig. 4. (a) Electron temperature and density profile from TVTS prior to the sawtooth phase and 40 ms before the first internal disruption appeared in Fig. 3. (b) Electron temperature and density profile during the sawtooth phase 40 ms after the first internal disruption.

Fig. 5. Time evolution of visible bremsstrahlung line-integrated intensity (a) and the Abel-inverted emissivity (b) profile.

Fig. 6. (a) The Z_{eff} profile measured by visible bremsstrahlung at the times of the plasma profiles in Fig. 4. The smooth curves indicate Z_{eff} profiles calculated with the impurity transport model for different values of C_v. Solid lines are best fits, and dashed lines are estimated upper and lower limits. The sawtooth model is used in the transport model in case (b), with D = 10^4 cm^2/s, mixing radius r_{mix} = 20 cm, and sawtooth period t_{saw} = 10 ms.

Fig. 7. Impurity density profiles for each charge state just before (a) and after (b) internal disruptions used in the flattening model in the MIST code. The total number of particles for each charge state within the mixing radius (r_{mix} = 20 cm) is conserved. The example shown is for nickel, assuming typical n_e and T_e profiles for PBX and c_v = 4.

Fig. 8. Sensitivity of the average Z_{eff} profile to the redistributed ion profile at internal disruption in the sawtooth model for c_v = 4.0, D = 10^4 cm^2/s, t_{saw} = 10 ms, and r_{mix} = 20 cm. Case I is flat redistributed profile used in this analysis. Case II and Case III are Gaussian redistributed profiles with their centers at r_{mix} and half widths of r_{mix} and $r_{mix}/2$, respectively.

Fig. 9. Decay of Ni XVII (249.2 Å) and Ni XVIII (292.0 Å) line-integrated emission during impurity decay phase. Transport coefficients used in the model calculations: c_v = 11.0, D = 10^4 cm^2/s before MHD onset (t < 485 ms); c_v = 6.5, 4.0, 2.5, D = 10^4 cm^2/s, t_{saw} = 10 ms and r_{mix} = 20 cm (in the first sawteeth r_{mix} = 10, 15 cm, respectively) at t > 485 ms. Open circles are 20-ms averaged intensities measured by VUV spectroscopy.

Fig. 10. The allowed range of combinations of peaking parameter c_v and diffusion coefficient D in sawtooth discharges as determined by the Z_{eff} profile and the decay of Ni XVII and Ni XVIII emissions. The shaded area indicates the allowed overlap region for c_v, D pairs to be consistent with the data within a reasonable error estimate.

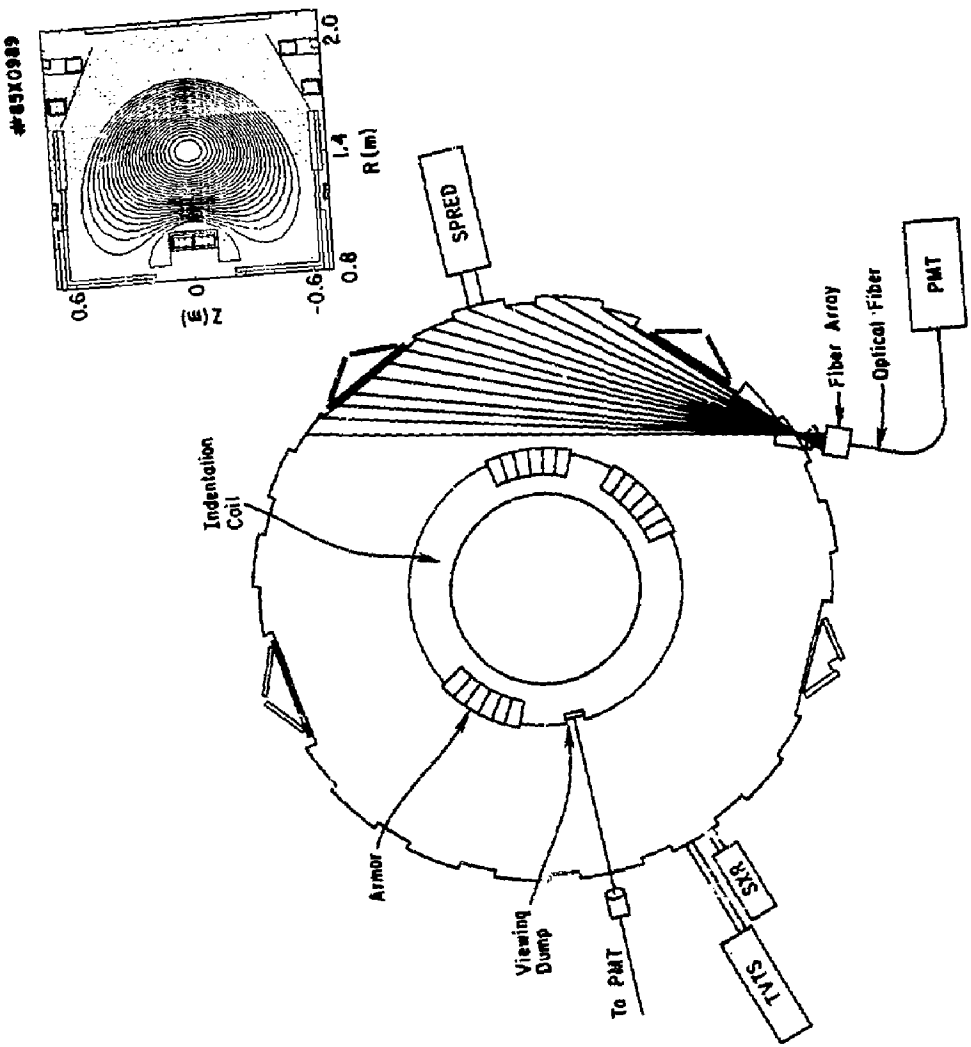
#85X0989
2.0
1.4
R(m)
0.8
-0.6
0
Z(m)
0.6
SPRED
Fiber Array
Optical Fiber
PMT
Indentation Coil
Armor
Viewing Dump
To PMT
SXR
TVTS

Fig. 1

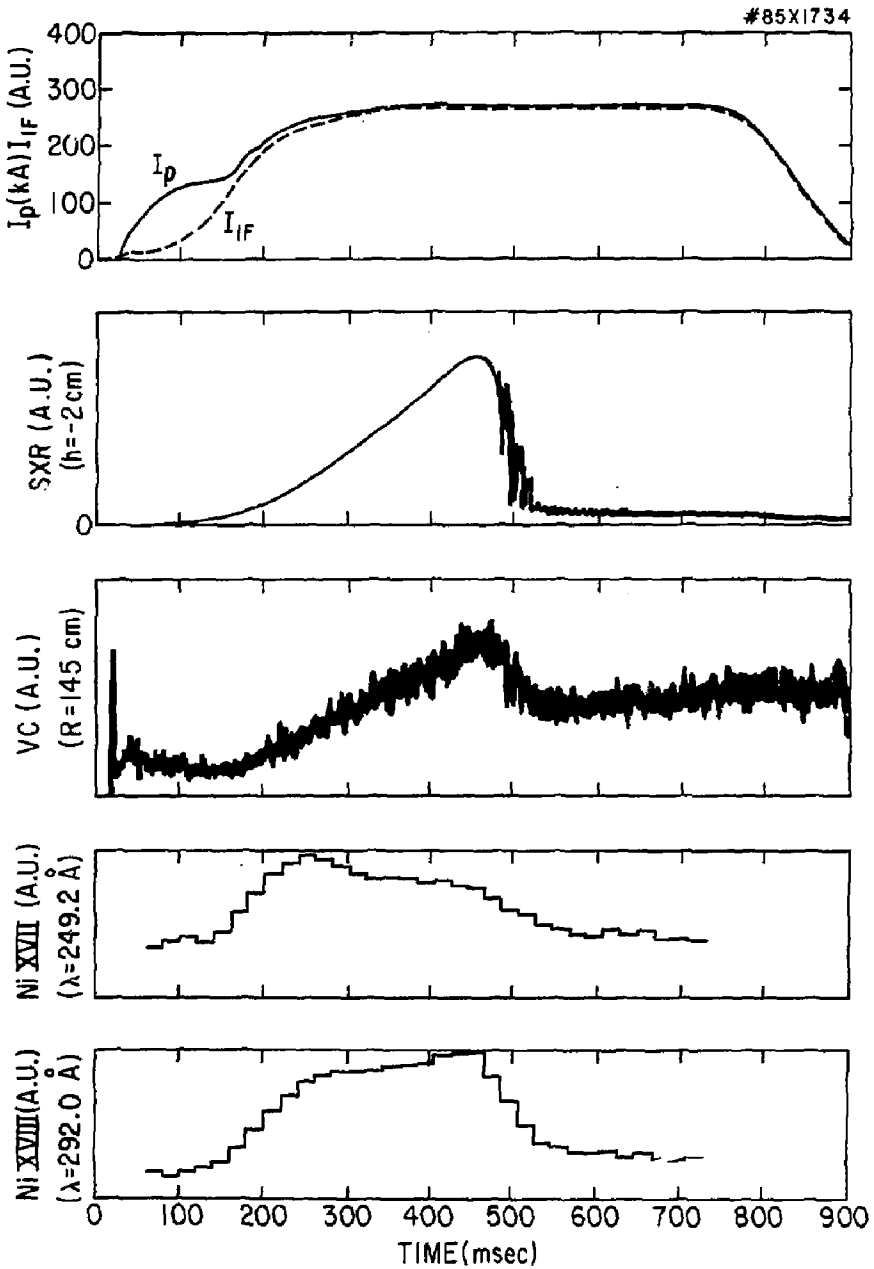
#85X1734
400
300
200
100
0
I_p(kA) I_{1F} (A.U.)
I_p
I_{1F}
SXR (A.U.)
(h=-2cm)
0
VC (A.U.)
(R=145 cm)
Ni XVII (A.U.)
(λ=249.2 Å)
Ni XVIII(A.U.)
(λ=292.0 Å)
0
100
200
300
400
500
600
700
800
900
TIME(msec)

Fig. 2

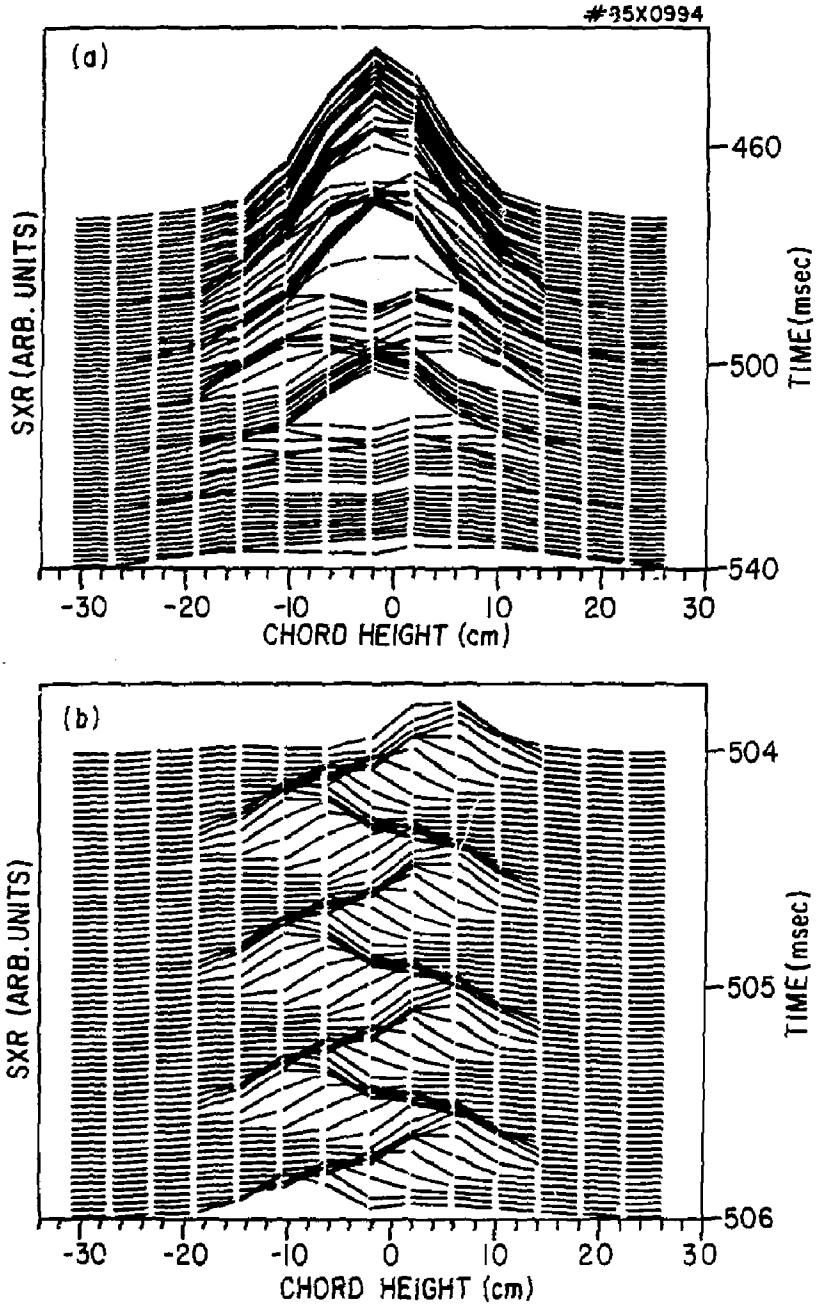
#35X0994
(a)
SXR (ARB. UNITS)
460
500
540
TIME (msec)
-30
-20
-10
0
10
20
30
CHORD HEIGHT (cm)
(b)
SXR (ARB. UNITS)
504
505
506
TIME (msec)
-30
-20
-10
0
10
20
30
CHORD HEIGHT (cm)

Fig. 3

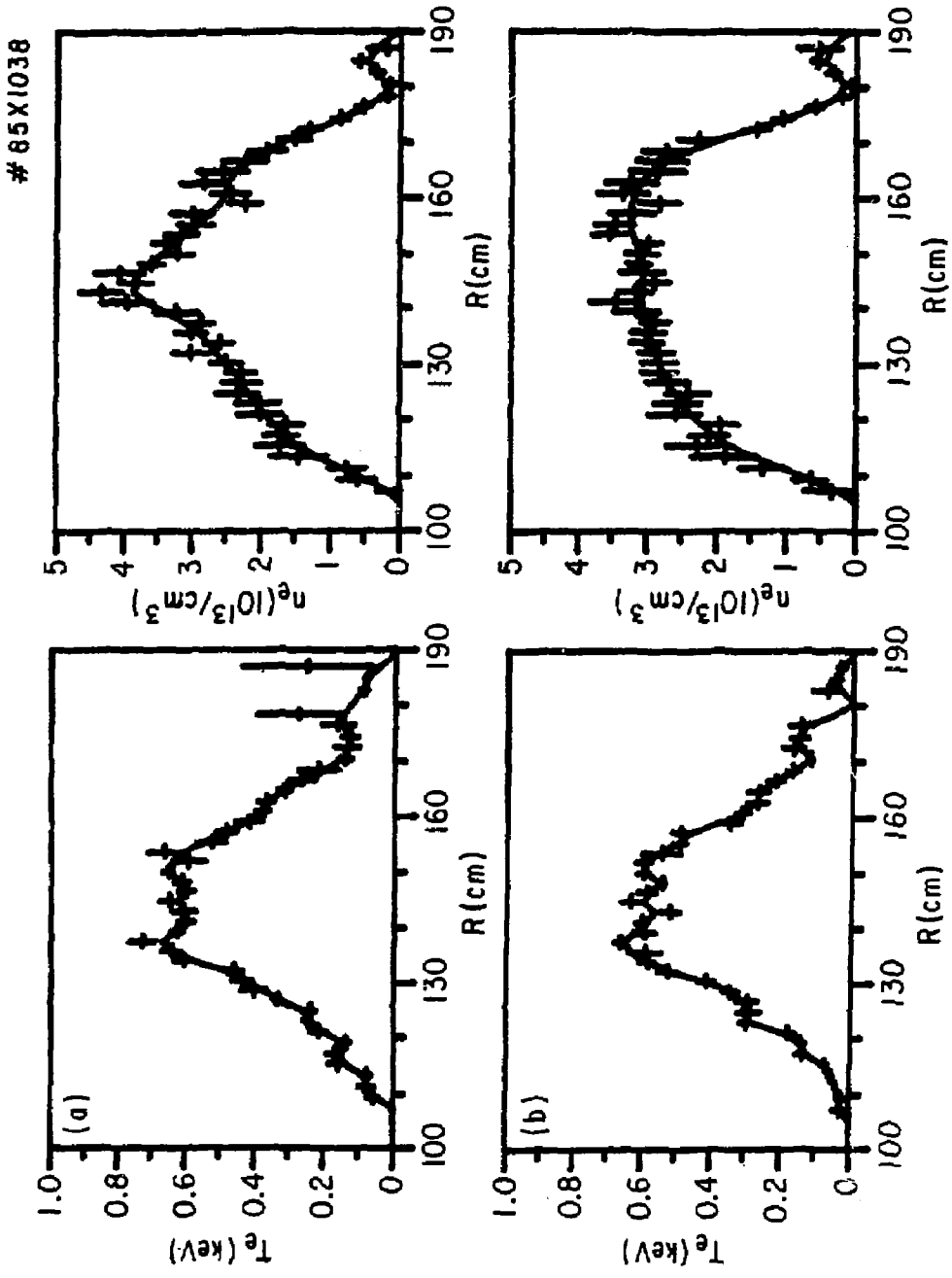
#85X1038
(a)
(b)
T_e (keV)
$n_e(10^{13}/cm^3)$
R(cm)
0
0.2
0.4
0.6
0.8
1.0
1
2
3
4
5
100
130
160
190

Fig. 4

#85X1229

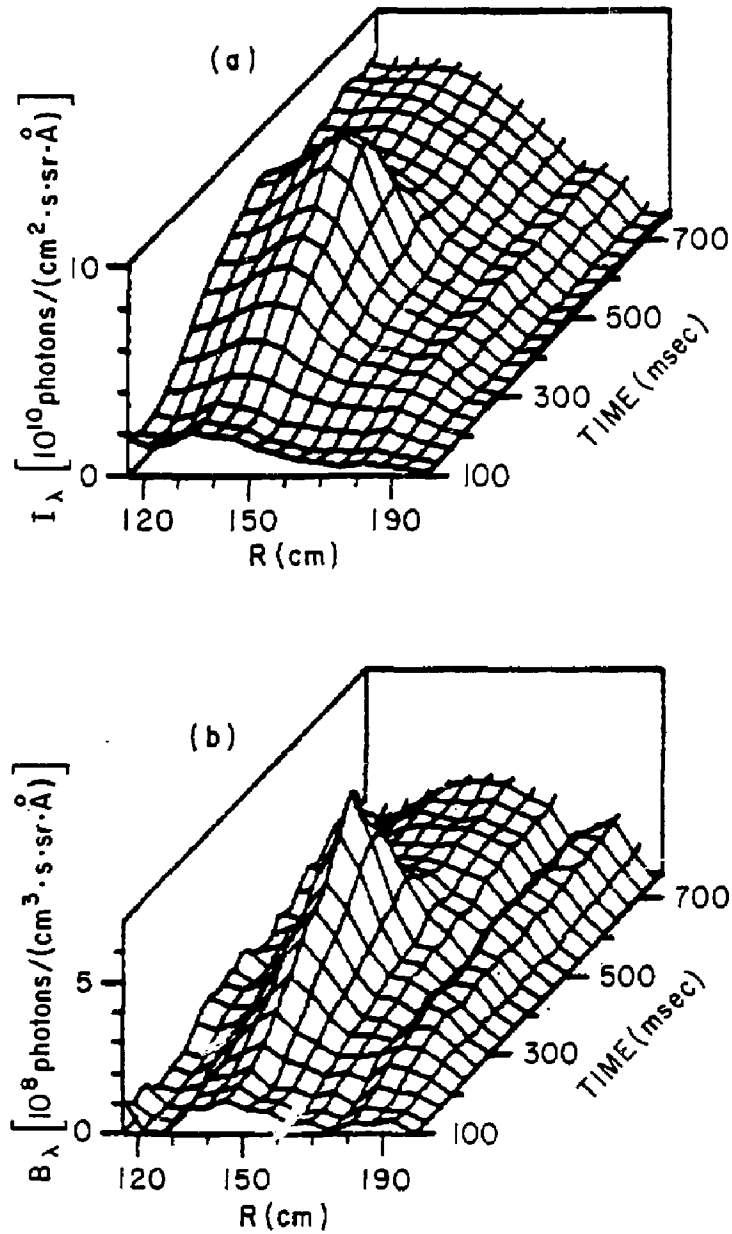

Fig. 5

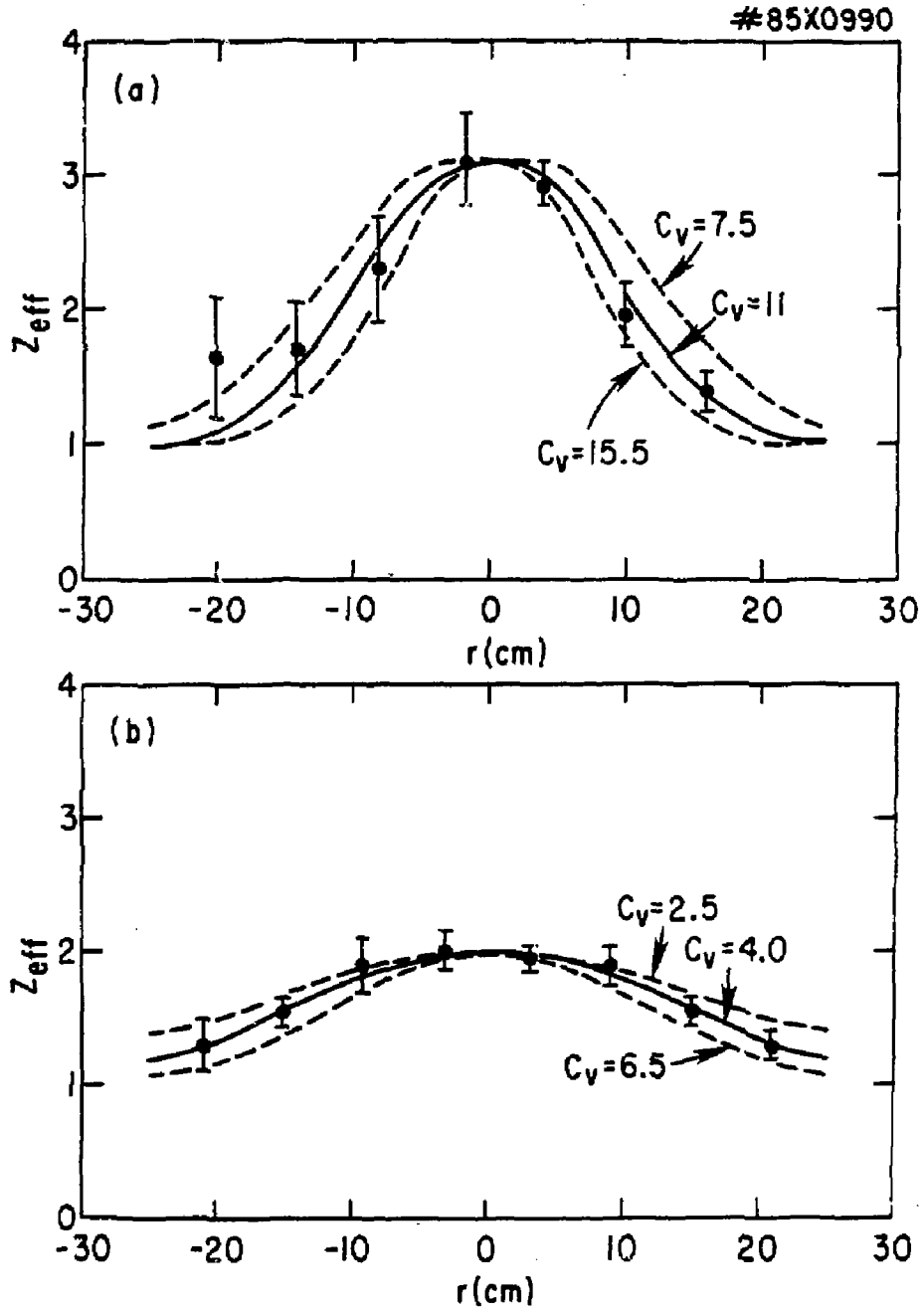

Fig. 6

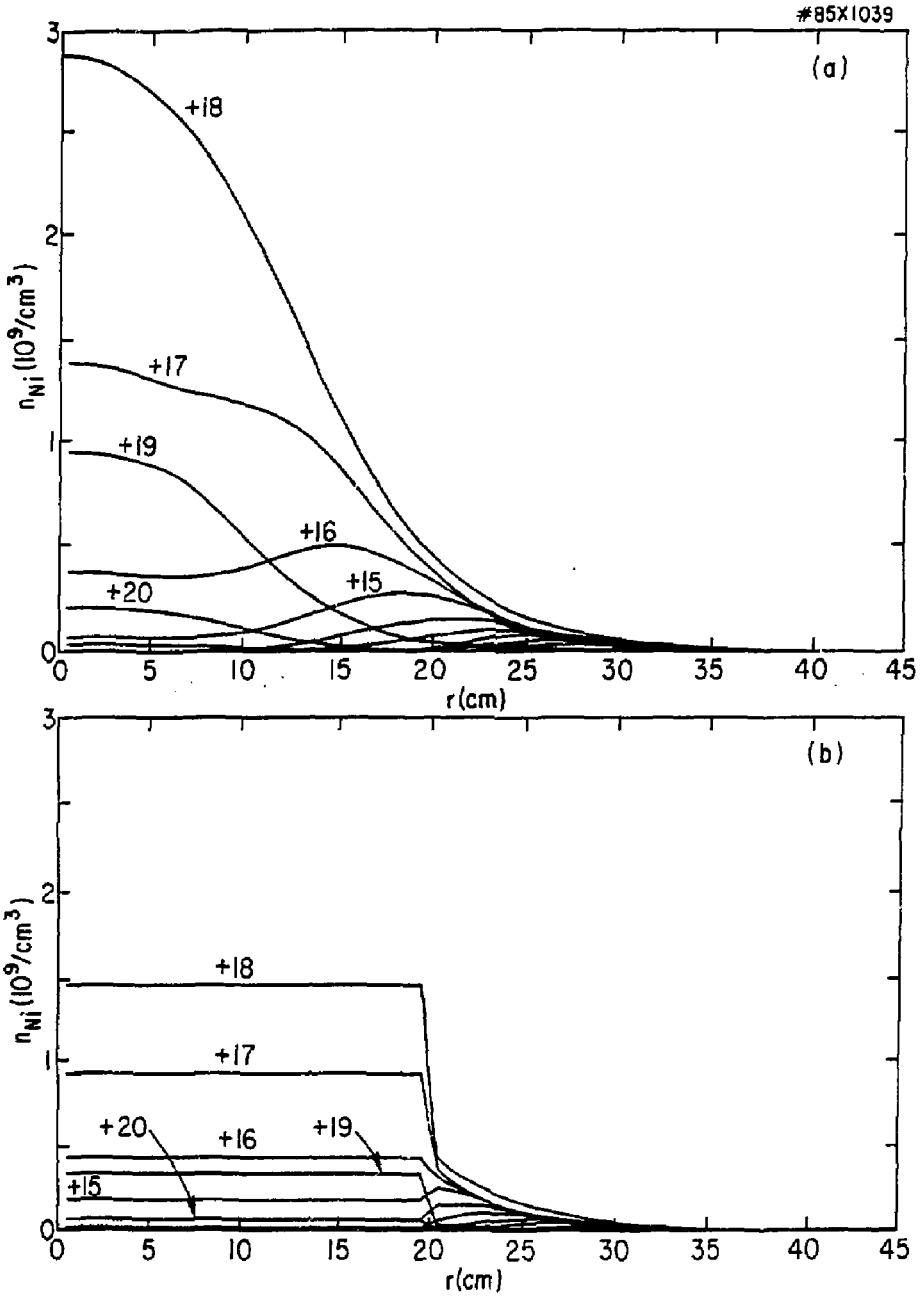
#85X1039
(a)
+18
+17
+19
+16
+20
+15
$n_{Ni}(10^9/cm^3)$
r(cm)
(b)
+18
+17
+20
+16
+19
+15
$n_{Ni}(10^9/cm^3)$
r(cm)

Fig. 7

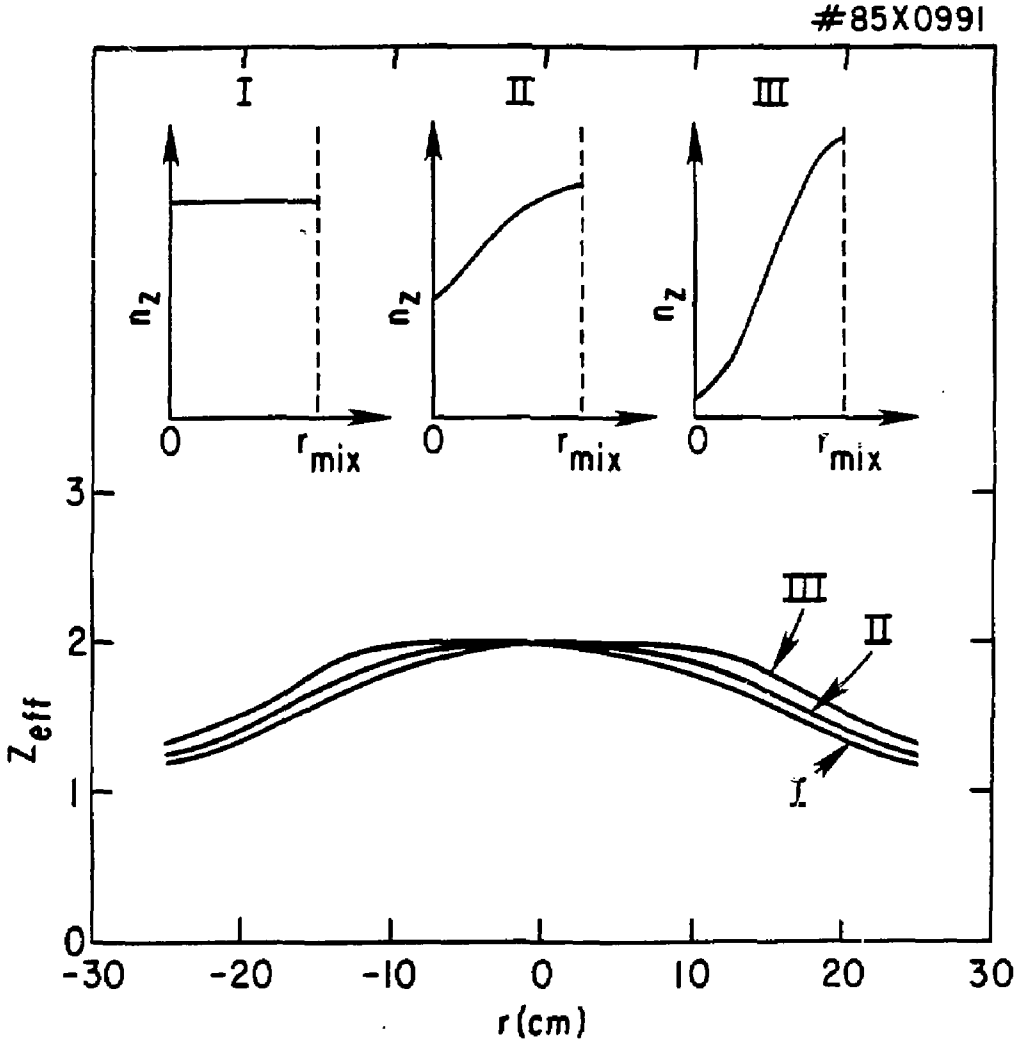

Fig. 8

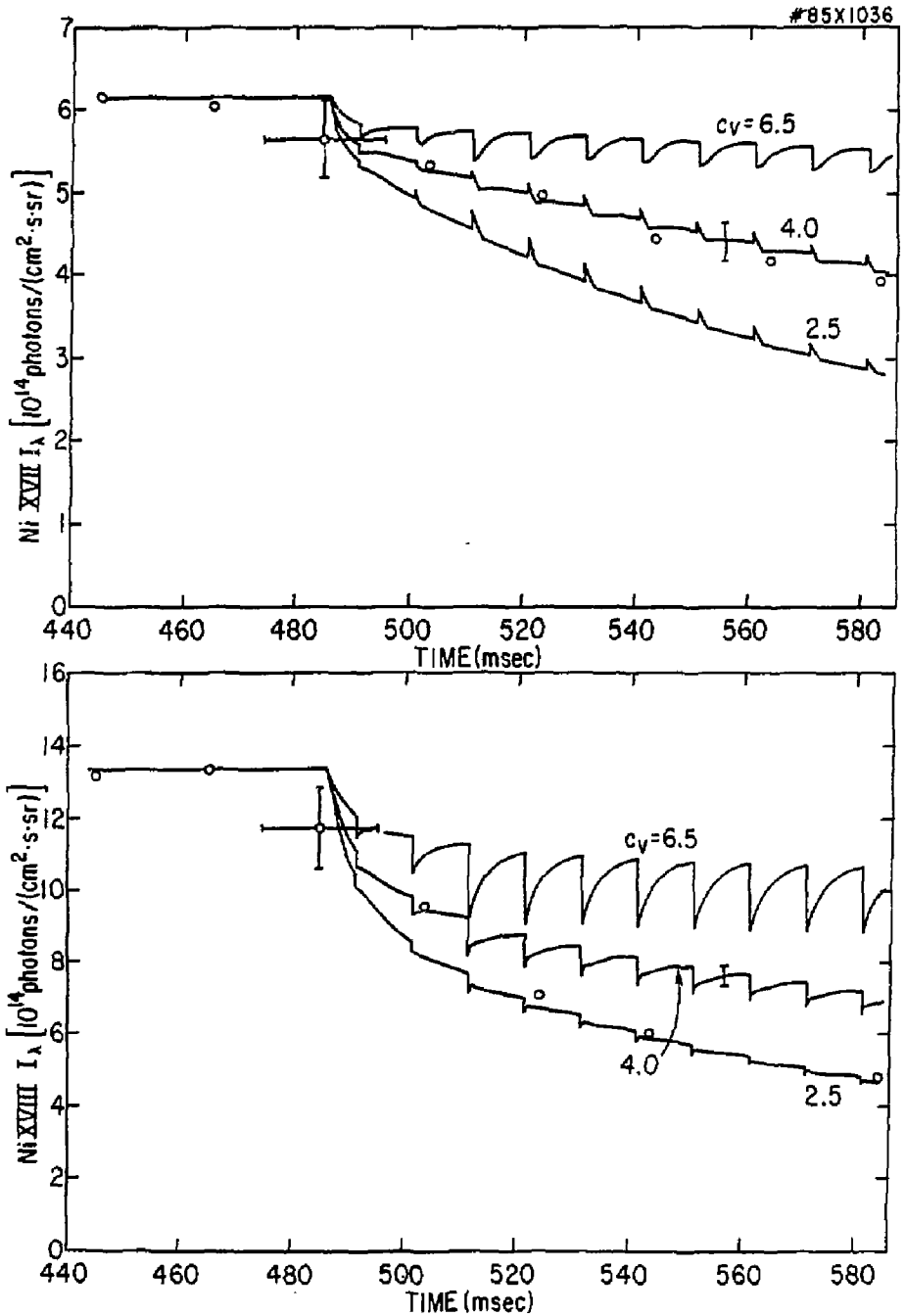
#85X1036
Ni XVIII I_λ [10^{14}photons/(cm^2·s·sr)]
c_V=6.5
4.0
2.5
TIME(msec)
NiXVIII I_λ [10^{14}photons/(cm^2·s·sr)]
c_V=6.5
4.0
2.5
TIME (msec)

Fig. 9

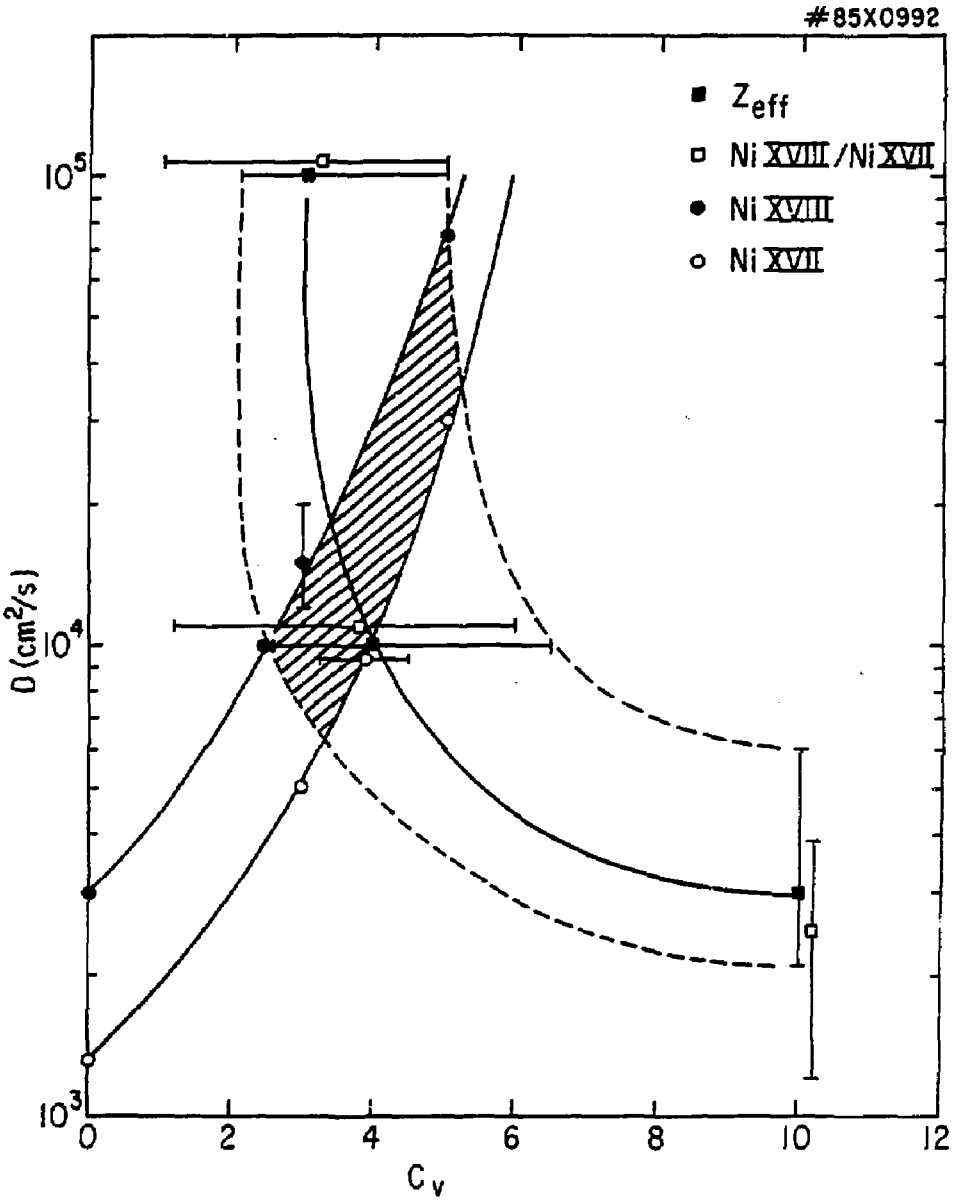
#85X0992
Z_{eff}
Ni XVIII/Ni XVII
Ni XVIII
Ni XVII
10^5
10^4
10^3
D (cm²/s)
0
2
4
6
8
10
12
C_v

Fig. 10

EXTERNAL DISTRIBUTION IN ADDITION TO UC-20

Plasma Res Lab, Austra Nat'l Univ, AUSTRALIA
Dr. Frank J. Paoloni, Univ of Wollongong, AUSTRALIA
Prof. I.R. Jones, Flinders Univ., AUSTRALIA
Prof. M.H. Brennan, Univ Sydney, AUSTRALIA
Prof. F. Cap, Inst Theo Phys, AUSTRIA
Prof. Frank Verheest, Inst theoretische, BELGIUM
Dr. D. Palumbo, Dg XII Fusion Prog, BELGIUM
Ecole Royale Militaire, Lab de Phys Plasmas, BELGIUM
Dr. P.H. Sakanaka, Univ Estadual, BRAZIL
Dr. C.R. James, Univ of Alberta, CANADA
Prof. J. Teichmann, Univ of Montreal, CANADA
Dr. H.M. Skarsgard, Univ of Saskatchewan, CANADA
Prof. S.R. Sreenivasan, University of Calgary, CANADA
Prof. Tudor W. Johnston, INRS-Energie, CANADA
Dr. Hannes Barnard, Univ British Columbia, CANADA
Dr. M.P. Bachynski, MPB Technologies, Inc., CANADA
Chalk River, Nucl Lab, CANADA
Zhengwu Li, SW Inst Physics, CHINA
Library, Tsing Hua University, CHINA
Librarian, Institute of Physics, CHINA
Inst Plasma Phys, Academia Sinica, CHINA
Dr. Peter Lukac, Komenskeho Univ, CZECHOSLOVAKIA
The Librarian, Culham Laboratory, ENGLAND
Prof. Schatzman, Observatoire de Nice, FRANCE
J. Radet, CEN-BP6, FRANCE
AM Dupas Library, AM Dupas Library, FRANCE
Dr. Tom Mual, Academy Bibliographic, HONG KONG
Preprint Library, Cent Res Inst Phys, HUNGARY
Dr. R.K. Chhajlani, Vikram Univ. INDIA
Dr. B. Dasgupta, Saha Inst, INDIA
Dr. P. Kaw, Physical Research Lab, INDIA
Dr. Phillip Rosenau, Israel Inst Tech, ISRAEL
Prof. S. Cuperman, Tel Aviv University, ISRAEL
Prof. G. Rostagni, Univ Di Padova, ITALY
Librarian, Int'l Ctr Theo Phys, ITALY
Miss Clelia De Palo, Assoc EURATOM-ENEA, ITALY
Biblioteca, del CNR EURATOM, ITALY
Dr. H. Yamato, Toshiba Res & Dev, JAPAN
Direc. Dept. Lg. Tokamak Dev. JAERI, JAPAN
Prof. Nobuyuki Inoue, University of Tokyo, JAPAN
Research Info Center, Nagoya University, JAPAN
Prof. Kyoji Nishikawa, Univ of Hiroshima, JAPAN
Prof. Sigeru Mori, JAERI, JAPAN
Prof. S. Tanaka, Kyoto University, JAPAN
Library, Kyoto University, JAPAN
Prof. Ichiro Kawakami, Nihon Univ, JAPAN
Prof. Satoshi Itoh, Kyushu University, JAPAN
Dr. D.I. Choi, Adv. Inst Sci & Tech, KOREA
Tech Info Division, KAERI, KOREA
Bibliotheek, Fom-Inst Voor Plasma, NETHERLANDS
Prof. B.S. Liley, University of Waikato, NEW ZEALAND
Prof. J.A.C. Cabral, Inst Superior Tecn, PORTUGAL
Dr. Octavian Petrus, ALI CUZA University, ROMANIA
Prof. M.A. Hellberg, University of Natal, SO AFRICA
Dr. Johan de Villiers, Plasma Physics, Nucor, SO AFRICA
Fusion Div. Library, JEN, SPAIN
Prof. Hans Wilhelmson, Chalmers Univ Tech, SWEDEN
Dr. Lennart Stenflo, University of UMEA, SWEDEN
Library, Royal Inst Tech, SWEDEN
Centre de Recherchesen, Ecole Polytech Fed, SWITZERLAND
Dr. V.T. Tolok, Kharkov Phys Tech Ins, USSR
Dr. D.D. Ryutov, Siberian Acad Sci, USSR
Dr. G.A. Eliseev, Kurchatov Institute, USSR
Dr. V.A. Glukhikh, Inst Electro-Physical, USSR
Institute Gen. Physics, USSR
Prof. T.J.M. Boyd, Univ College N Wales, WALES
Dr. K. Schindler, Ruhr Universitat, W. GERMANY
Nuclear Res Estab, Julich Ltd, W. GERMANY
Librarian, Max-Planck Institut, W. GERMANY
Bibliothek, Inst Plasmaforschung, W. GERMANY
Prof. R.K. Janev, Inst Phys, YUGOSLAVIA